

Enhancing Chemical Stability and Suppressing Ion Migration in $\text{CH}_3\text{NH}_3\text{PbI}_3$ Perovskite Solar Cells *via* Direct Backbone Attachment of Polyesters on Grain Boundaries

Yuchen Zhou, Yifan Yin, Xianghao Zuo, Likun Wang, Tai-De Li, Yuanyuan Zhou, Nitin P. Padture, Zhenhua Yang, Yichen Guo, Yuan Xue, Kim Kisslinger, Mircea Cotlet, Chang-Yong Nam,* and Miriam H. Rafailovich*

Cite This: *Chem. Mater.* 2020, 32, 5104–5117

Read Online

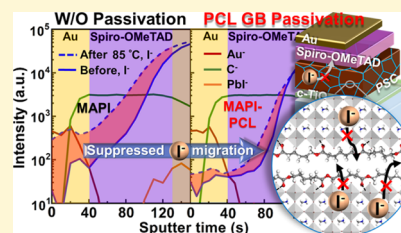
ACCESS |

Metrics & More

Article Recommendations

Supporting Information

ABSTRACT: Organic–inorganic halide perovskites feature excellent optoelectronic properties but poor chemical stability. While passivating perovskite grain boundary (GB) by polymers shows prospects on long-term performance of perovskite solar cells (PSCs), its detailed impact on the ion migration phenomenon, which largely deteriorates the PSC stability, remains less probed. Here, we introduce a new polar polymer, polycaprolactone (PCL), to passivate GBs of methylammonium lead triiodide (MAPbI_3) perovskite with only 1–2 polymer monolayers *via* direct backbone attachment. The PSCs with passivated MAPbI_3 , using a classic but less stable Spiro-OMeTAD (2,2',7,7'-tetrakis[*N,N*-di(4-methoxyphenyl)amino]-9,9'-spirobifluorene) hole transport layer (HTL), exhibit improved power conversion efficiencies up to 20.1%, with 90% of the initial PCE being preserved after 400 h ambient storage, and 80% even after 100 h, 85 °C aging. The improved PSC stability indicates critical roles of PCL GB passivation in retarding moisture-induced decomposition and suppressing ion migration within the perovskite. Time-of-flight secondary ion mass spectrometry reveals that I^- ions can actively migrate into the electrode, HTL, and their interface in nonpassivated PSCs, even without an externally applied electric field, while such migration is significantly mitigated in PCL-passivated PSCs. This effective GB passivation by PCL suggests an important potential of polymer additives toward the development of stable high-performance PSCs.



INTRODUCTION

The interest in organic–inorganic halide perovskite (OIHP) materials for use in next-generation thin-film perovskite solar cells (PSCs)¹ has risen dramatically since 2009² owing to the rapid rise in the power conversion efficiency (PCE) of PSCs. Methylammonium lead triiodide ($\text{CH}_3\text{NH}_3\text{PbI}_3$ or MAPbI_3) is the most popular OIHP used in PSCs^{3–5} because of its excellent optoelectronic properties, such as high absorption coefficient,⁶ wide absorption range, low exciton binding energy,⁷ long electron and hole diffusion lengths,^{4,8} high ambipolar charge mobilities,⁹ and extended charge carrier lifetime.^{1,10} Despite the high PCE and excellent optoelectronic properties, MAPbI_3 (MAPI)-based OIHPs suffer from poor structural and chemical stability because of the tendency of the MAPI to decompose into non-photoactive PbI_2 when exposed to environmental conditions such as ambient moisture and heat.^{11,12} Furthermore, the MAPI-based PSCs can undergo rapid performance degradation, especially under applied electric fields with illumination, because of ion migration and its accumulation at the device interfaces.^{13–16} These stability issues are serious obstacles that must be overcome for MAPI-based PSCs to reach their full potential.

OIHP thin films in PSCs are invariably polycrystalline, and it is well established that the degradation of the MAPI thin films in

PSCs is mediated by the grain boundaries (GBs), which provide pathways for the rapid ingress of moisture and oxygen from the environment.^{17–19} Once the degradation is initiated, it can then spread to the entire grains, eventually decomposing the entire thin film.^{12,17,18} It is also known that GBs allow fast diffusion of ionic species,^{20–22} thus facilitating the detrimental ion migration in PSCs. One strategy to slow halide migration has been to chemically modify the perovskite by mixing halides,²³ as mixed-halide systems have displayed lower interdiffusion and migration than their single halide-based counterparts.^{23–25} While such mixed-halide systems have displayed enhanced device performance,²³ mixing halides invariably changes the perovskite bandgap, and GBs still remain.^{23–25} Another approach was devoted toward increasing the grain size and, thus, reducing the GB density in MAPI thin films by identifying proper solvents and developing spin-casting techniques.^{5,26–29} While these approaches have been effective in producing coarse-grained

Received: March 6, 2020

Revised: May 22, 2020

Published: May 22, 2020



MAPI thin films, and enhancing PSC performance and stability as a result, the existing GBs still provide rapid conduits for film degradation. An alternative approach that is being developed is the passivation of the GBs by using additives to effectively retard the ingress of moisture and oxygen and ion migration.^{30–35} While this strategy has shown promising results, the choice of additives and the control of the associated passivation effect have been greatly limited by their solubility in the precursor solvents, such as dimethyl sulfoxide (DMSO), *N,N*-dimethylformamide (DMF), or γ -butyrolactone. This is because the additives effecting GB passivation usually need to be solubilized together with the perovskite precursors when the thin films are solution processed to ensure the uniform distribution of the additives and the smoothness of the films.

One of the main approaches under the current investigation is the addition of soluble organic polymers,^{12,35–44} a class of macromolecules wherein numerous chemical architectures are available. In principle, they can be designed to provide not only hydrophobic interactions for reduced moisture adsorption at OIHP GBs but also strong binding interacting with the OIHP grains for reduced ion dissociation and migration. Furthermore, soluble polymers can be directly incorporated into the spin-cast films through its precursor solution without further modifications of the existing thin-film processing and device fabrication protocols.⁴⁵

One of the first uses of macromolecular additives was reported by Bi *et al.*,³⁶ who incorporated commercially available poly(methyl methacrylate) (PMMA) homopolymers into the perovskite layer. Later, Zuo *et al.*³⁸ reported using polymers with functional branches such as polyethylenimine, polyvinylpyrrolidone, or polyvinyl alcohol. Both reported improvements in PCE, which were attributed to the formation of coordinating adducts between the polymers and the OIHP grains. However, the location of the polymer within the OIHP layer was not clearly identified, and the enhancement of environmental stability was not systematically demonstrated. More recently, Zong, *et al.*¹² blended polyethylene oxide–poly(*p*-phenylene oxide)–polyethylene oxide (PEO–PPO–PEO) co-polymers into the MAPI thin films and, using transmission electron microscopy (TEM), showed the continuous functionalization of GBs by the polymer. As a result, the PSCs made from such MAPI thin films showed not only enhanced PCE but also improved stability under continuous white light illumination and after 30-day storage in ambient air.¹² Nevertheless, these studies did not discuss the effects of polymer incorporation on the ion migration, which is especially important in typical *n–i–p* device structures that use popular Spiro-OMeTAD (2,2',7,7'-tetrakis-[*N,N*-di(4-methoxyphenyl)amino]-9,9'-spirobifluorene) as the hole transport layer (HTL). These architectures can usually generate high PCEs, but their performance is known to be sensitive to ion (iodine) migration and aggregation into the HTL and at the electrode-HTL interface. At the HTL interface, the penetration of iodine ions prevents the oxidation of Spiro-OMeTAD, reducing its *p*-doped characteristics and degrading its electrical properties,^{46,47} while at the back-contact electrodes (typically made of Ag), corrosion can occur from chemical reactions between the Ag electrode and the migrated iodide ions.^{21,46,48} Both lead to the degradation of the photovoltaic (PV) performance of the *n–i–p* PSCs.

Here, we report the use of a new polymer additive, polycaprolactone (PCL), which can have strong binding interactions with perovskite GBs through unique, direct *backbone* attachments unlike reported polymer addi-

tives,^{36–38,43,44} where the polymer–perovskite interaction was realized by *peripheral* branch groups of polymer chains. *Via* this approach, we demonstrate not only an increased PCE of PSCs with enhanced open circuit voltage (V_{OC} of 1.145 V with 20.1% PCE), but also, more importantly, significantly increased combined chemical stabilities of perovskites against moisture, heat, and light, realizing the preservation of more than 90% of the initial PCE of *n–i–p* PSCs when exposed to moisture for 400 h and 80% of the initial PCE after the exposure to heat for roughly 100 h. The passivation of MAPI GBs by PCL was probed and confirmed using multiple complementary techniques, revealing the structure of PCL passivation of GBs and its effects on the stability and ion migration within the perovskite and its PSCs. The location of the PCL polymer on MAPI GBs was clearly visualized using high-resolution TEM, as well as the lateral force (friction mode) atomic force microscopy (AFM). Using the dynamic time-of-flight secondary ion mass spectroscopy (ToF-SIMS) technique, we were able to accurately measure the decrease in iodide ion migration in the *n–i–p* structured PSCs by the PCL GB passivation, which largely contributes to the improved PV stability of *n–i–p* PSCs using Spiro-OMeTAD as an HTL.

EXPERIMENTAL SECTION

Materials. PbI₂ (99.99% trace metal basis) was purchased from TCI Chemicals. PCL polymer with a narrow distribution (polydispersity of 1.18) was purchased from Polymer Source, Inc. All other materials, including methylammonium iodide (MAI, anhydrous 99%), DMF (anhydrous 99.8%), DMSO (anhydrous 99.9%), toluene, and fluorine-doped tin oxide (FTO) glass (TEC 7) were purchased from Sigma-Aldrich. All chemicals were used as received without further purification.

Fabrication of MAPI PSCs. The FTO glasses were sonicated sequentially in ethanol, isopropanol, and acetone. The cleaned FTO glasses were then coated with 40–50 nm thick compact TiO₂ (*c*-TiO₂) *via* spin-casting of its precursor solution as reported previously⁴⁹ at 3000 rpm for 20 s, followed by pyrolysis at 450 °C for 2 h with 1 h cooling step afterward. An UV–ozone treatment was performed for 10 min on *c*-TiO₂ coated substrates before casting the perovskite precursor solution. The precursor solution with a concentration of 1.2 M MAI and PbI₂ (molar ratio of 1:1) was prepared by dissolving 553 mg of PbI₂ and 190 mg of MAI in the mixed solvents of 0.9 mL of DMF and 0.1 mL of DMSO. Varying amounts of the PCL polymer were then dissolved into the solution after fully dissolving MAI and PbI₂. All solutions (with and without PCL) were heated at 60–70 °C for 30 min to ensure a full dissolution of solids and obtain a crystal-clear solution before being spin-casted onto *c*-TiO₂ coated FTO glasses (Figure S1). A uniform perovskite layer was fabricated by first drop-casting the perovskite precursor solution onto *c*-TiO₂ coated FTO glass followed by spin-drying at 4000 rpm for 30 s. Immediately after 10 s of spinning, 150 μ L of toluene was added onto the rotating substrate surface as an antisolvent. The precursor-coated FTO glass substrate was then transferred to a hot plate for annealing at 100 °C for 10 min to finally form a brownish-black MAPI layer with a highly smooth surface. To prepare the HTL, a Spiro-OMeTAD solution with additives was first prepared by dissolving 80 mg of Spiro-OMeTAD, 20 μ L of 500 mg/mL stock solution of Li-bis(trifluoromethanesulfonyl)imide (LiTFSI) in acetonitrile, and 30 μ L of 4-*tert*-butylpyridine (tBP) in 1 mL of chlorobenzene. The hole-conductive Spiro-OMeTAD layer was then coated onto the MAPI perovskite surface *via* spin-casting at 4000 rpm for 30 s. Finally, 60 nm thick Au electrodes were deposited onto the Spiro-OMeTAD surface *via* electron beam evaporation through a shadow mask.

Structure Characterizations. The surface and grain structure of MAPI films were characterized by scanning electron microscopy (SEM, Hitachi S-4800) at an acceleration voltage of 2 kV. The friction information of the surface of MAPI thin films with and without the PCL

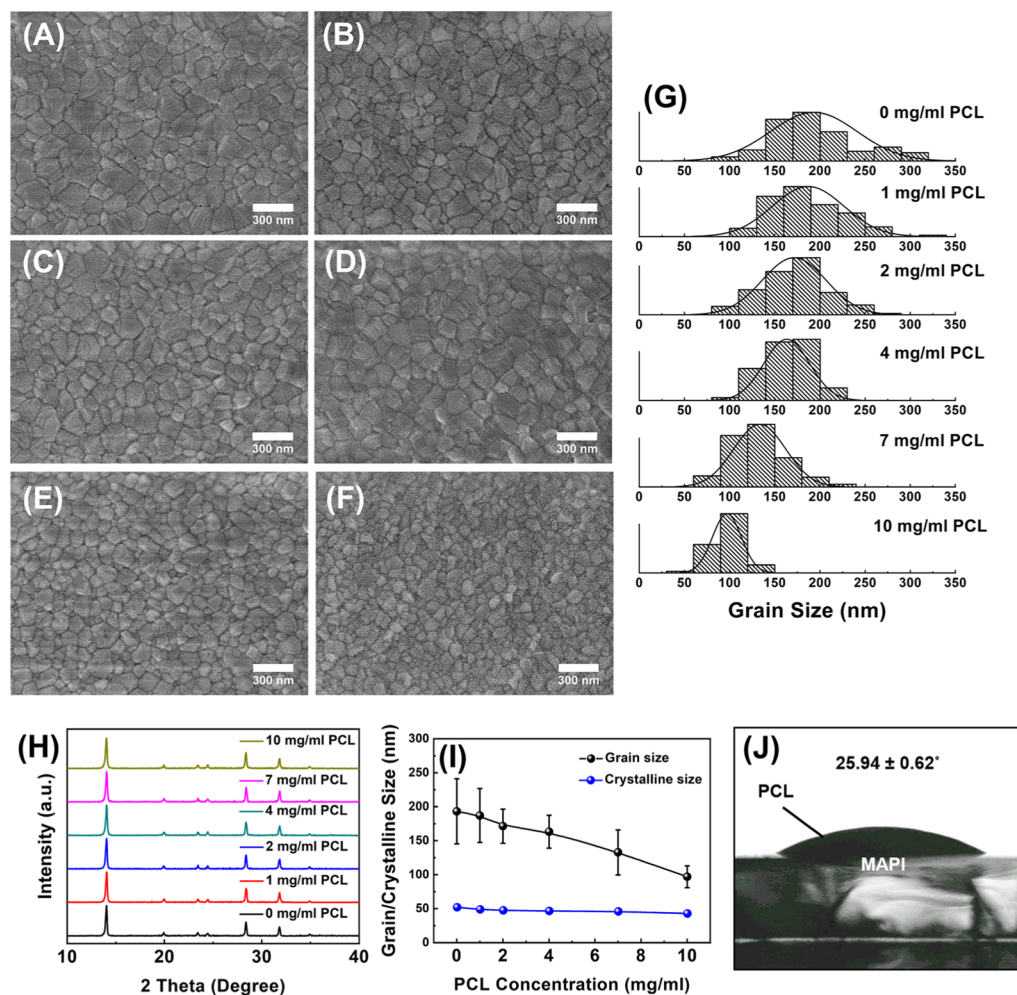


Figure 1. Microstructure of PCL-incorporated MAPI perovskite thin films. Top-view SEM images of MAPI films with 0 (A), 1 (B), 2 (C), 4 (D), 7 (E), and 10 mg/mL (F) of PCL incorporation. (G) Grain size distribution with respect to the PCL concentration in the MAPI film. (H) XRD spectra obtained from MAPI thin films with various amounts of PCL. (I) PCL-concentration-dependent variation of the perovskite grain size determined from SEM (black) and the crystallite size determined from XRD (blue). (J) Photograph of a melted PCL droplet on the perovskite surface used for the contact angle measurement.

polymer was acquired by the contact-mode AFM (Bruker Dimension 3000). X-ray diffractometry (XRD, Rigaku Ultima III) was used to characterize the crystal structure of thin film MAPI perovskites by using the Bragg–Brentano geometry with a 2θ range from 10 to 40° , sampling width of 0.04° , and scan rate of $3^\circ/\text{min}$ under operation conditions of 44 kV and 40 mA. Detailed atomic-scale grain structures of MAPI thin films were examined by TEM (JOEL 1400 with acceleration voltage of 80 kV and FEI Talos with acceleration voltage of 200 kV). TEM samples were prepared by spin-casting the diluted perovskite precursor solution onto holey carbon TEM grids, which were then annealed at 100°C for 10 min. This sample preparation method may avoid the damage of the samples from other methods, such as focused ion beam preparation, and provide reliable characterization results.⁵⁰ Chemical characteristics of perovskite samples were characterized by attenuated total reflectance–Fourier transform infrared spectroscopy (ATR–FTIR, Thermo, Nicolet 6700), polarization modulation-infrared reflection-adsorption spectroscopy (PM-IRRAS, home-built), and X-ray photoemission spectroscopy (XPS, Physical Electronics VersaProbe II). For ATR–FTIR, powders were prepared by scraping perovskite films off from 3 substrates, and FTIR spectra were recorded in transmittance mode. For PM-IRRAS, the samples were prepared by spin-casting perovskite films onto the Au-coated Si substrate. XPS was performed using Al $K\alpha$ X-ray, 45° take-off angle, and low-energy electron and Ar^+ surface charge compensation, under an ultra-high vacuum of 5×10^{-7} to 5×10^{-8} Pa, with 117.40 eV pass energy for high

resolution and 29.35 eV for survey spectra. The binding energy of the main C 1s peak at 284.8 eV (C–C or C–H) was used to correct the spectral shift caused by specimen surface charging.

Optical Property Characterizations. UV–visible absorption spectra of the perovskite thin films were obtained by using a UV–visible spectrophotometer (model Cary 60, Agilent, USA) with the scan range from 400 to 800 nm and a scan rate of 1000 nm/min. Steady-state photoluminescence (PL) of perovskite thin films were measured using a Fluorolog-Horiba fluorometer. Time-resolved PL experiments were performed using the time-correlated single photon counting spectroscopy by exciting the perovskite samples deposited on the c-TiO₂/glass substrate. The excitation wavelength for both steady-state and time-resolved PL was at 570 nm.

PV Performance Measurements. The PV performance of fabricated MAPI solar cells was tested by a modified PV probe station equipped with a 150 W solar simulator (Oriel, USA) with a air mass 1.5 global (AM1.5G) filter and precision semiconductor parameter analyzer (Agilent). The light intensity was calibrated to 100 mW cm^{-2} (1 sun) by a calibrated Si solar cell (Oriel) before each measurement. Current density–voltage (J – V) characteristics of devices with an active area of 0.12 cm^2 were recorded under illumination at a scan rate of 100 mV/s between 1.2 and 0 V. All as-prepared devices were kept in dry air (with desiccant) for the overnight oxidation of the Spiro-OMeTAD layer before measurements. Steady-state PCE measurements were carried out by recording the current

output of devices at the bias for the maximum power point with continuous 1 sun illumination for 120 s. External quantum efficiency (EQE) measurements were conducted using a home-built EQE setup composed of a 300 W xenon lamp (Oriel) and a monochromator (Oriel) attached to the PV probe station. All the PV measurements were performed in ambient air.

Stability Measurements. The chemical stability of PCL incorporated MAPI films were tested under several environmental stresses, including moisture, heat, and light, with all tested films prepared on c-TiO₂-coated FTO glass to emulate the actual PSC conditions. Specifically, the films were directly exposed to air with relative humidity (RH) around 70% for 24 h for the moisture stability test. To test the ability against extreme heat, the samples were heated at 100 °C in an Ar-filled atmosphere for 3 h. For the light stability experiment, a thin (50 nm) layer of PMMA was first spin-casted onto MAPI films to minimize the influence of other environmental factors. Then, light with AM1.5G 1 sun intensity was illuminated on the films for 20 h. The changes of the crystal structure in the films before and after the imposed environmental stresses were examined by XRD. The PCE stability of MAPI–PCL PSCs were tested by storing devices in air (dark, room temperature) with a controlled RH of 20–40%. *J*–*V* characteristics were then taken after certain periods of air storage. Before each measurement, the device was transferred to and kept in the Ar-filled glovebox for 20 min, and its surface was blow-dried with dry Ar to minimize the effects of surface moisture. The PCE stability was also probed after the thermal aging of PSCs at 85 °C in the glovebox. The devices were cooled down in the glovebox for 30 min before each measurement.

Ion Migration Characterizations. The impact of PCL on the ion migration within the perovskite layer was examined by measuring the composition depth profile *via* ToF-SIMS (PHI TRIFT V nano ToF-SIMS). ToF-SIMS was performed on PSCs with the Au or Ag electrode after storing them under Ar for a 48 h period and after additional thermal aging at 85 °C. The depth profiles of elements or ions of interest (*e.g.*, Au⁺, Ag⁺, I[−], C[−], PbI[−]) was measured by sputtering the perovskite film using 5 kV Ar gas gun (500 nA current, rastered over 800 μm × 800 μm area) and in sequence probing the composition of the exposed surface by using a 30 kV Bi⁺ liquid metal ion gun (LMIG) and analyzing sputtered negative secondary ions across 300 μm × 300 μm area. For each sputter–probe cycle, samples were sputtered for 5 or 10 s probing ions.

Charge Transport Activation Energy Measurement. The impact of PCL on the ion transport characteristics within the perovskite layer was examined by measuring the temperature-dependent current at a constant electrical bias and extracting the charge transport activation energy using a variable-temperature probe station (MMR) under vacuum (<10^{−4} Torr) equipped with a semiconductor parameter analyzer (Agilent). The perovskite devices with two top Au lateral in-plane electrodes (100 μm channel length and 1 mm width) were first cooled down to 120 K and heated to each target temperature (10 K/min heating rate) and stabilized for 10 min. The current was then measured after biasing the device at 20 V (corresponding electrical field of 0.2 V/μm) for 120 s.

RESULTS AND DISCUSSION

Microstructure of PCL-Incorporated MAPI Perovskite.

PCL-passivated MAPI perovskite thin films were prepared by the one-step spin casting procedure using a mixed solution containing MAI, PbI₂, and PCL polymer (as described in Supporting Information; Figure S1). Figure 1A–F shows SEM micrographs of the MAPI perovskite thin film with various concentration of incorporated PCL. The image analysis indicates that the average apparent grain size gradually decreases with increasing PCL concentration, from ~200 nm (pure MAPI) to 100 nm (10 mg/mL PCL), accompanied by a narrowed size distribution (Figure 1G). The crystal structure of perovskite thin films examined by XRD confirms that regardless of the amount of PCL, all samples exhibit a tetragonal structure

typical to MAPI perovskites (Figure 1H). Meanwhile, a Debye–Scherrer analysis of full-width-at-half-maxima of crystalline XRD peaks shows that the crystallite size remains relatively constant at ~50 nm with increasing PCL concentration despite the decreasing apparent grain size observed in SEM (Figure 1I). The smaller crystallite size compared with the apparent grain size suggests that each apparent grain observed in SEM contains multiple crystallites. It is noted that the PCL additive in MAPI films supports the increased nucleation of perovskite crystallites even without an antisolvent process as indicated by the increased perovskite film substrate coverage with the incorporation of PCL (Figure S2). Overall, these observations suggest that PCL does not affect the crystal structure of the perovskite but provides loci for increased heterogeneous nucleation of crystallites.

The surface coverage and roughness of perovskite films on substrates, which can be affected by process additives, are important factors influencing PSC performances.^{51–54} We find that the incorporation of PCL in MAPI ensures a good perovskite film coverage on substrates as PCL promotes heterogeneous nucleation of MAPI crystallites throughout the substrate. Moreover, under all tested incorporated PCL concentrations, MAPI thin films maintained the original, smooth, compact, and pinhole-free surface morphology without any visible polymer aggregation even at the highest concentrations studied (10 mg/mL), hinting good chemical affinity between the PCL and perovskite, which we confirm by more detailed studies of the chemical interaction in the later section. Consistently, the Young's contact angle (θ) formed when a droplet of PCL was molten on a pristine MAPI perovskite thin film in vacuum (Figure 1J) is relatively small ($\theta = 25.94^\circ$), indicating partial wetting^{55–58} of PCL on the MAPI perovskite surface and suggesting a possibility of the polymer being “wicked” into the intergranular channels during the nucleation and growth of MAPI crystallites and grains, thus passivating the perovskite GBs.

Chemical Interaction between the PCL Polymer and MAPI Perovskite. We investigated the chemical interaction between PCL and MAPI by comparing the molecular vibrational characteristics of PCL, pristine MAPI, and PCL-incorporated MAPI (2 mg/mL PCL) perovskite powder samples using ATR–FTIR (Figure 2). The primary “fingerprint” peak of PCL is located at 1720 cm^{−1} originating from the stretching of the C=O bond,^{59,60} while the broad peaks at 3168 and 3129 cm^{−1} associated with N–H stretching from MAPI^{61,62} are prominent for the pristine MAPI (Figure 2A). The PCL-incorporated MAPI features both the peaks from PCL and MAPI (Figure 2A), showing an apparent successful incorporation of PCL within the perovskite layer. Higher resolution spectra around the C=O stretching peak reveal more details of the chemical interaction between PCL and MAPI; after being mixed with MAPI, the C=O peak from PCL undergoes a blue shift from 1720 cm^{−1} to a higher wavenumber of 1725 cm^{−1} and broadening (Figure 2B). This is consistent with previous studies,^{30,38,63} which attributed these spectral changes to the coordination between C=O and Pb²⁺ *via* the electron donor (C=O)–acceptor (Pb²⁺) pair (*i.e.*, Lewis acid–base adduct) formation. A separate ATR–FTIR characterization of PCL, pristine PbI₂, and PCL-incorporated PbI₂ exhibited a similar blue shift of C=O vibration from 1720 to 1728 cm^{−1} (Figure 2C,D), further supporting the case of the chemical coordination between the PCL polymer and MAPI *via* the adduct formation between the C=O functional group of PCL and the Pb²⁺ of PbI₂ within the MAPI perovskite.

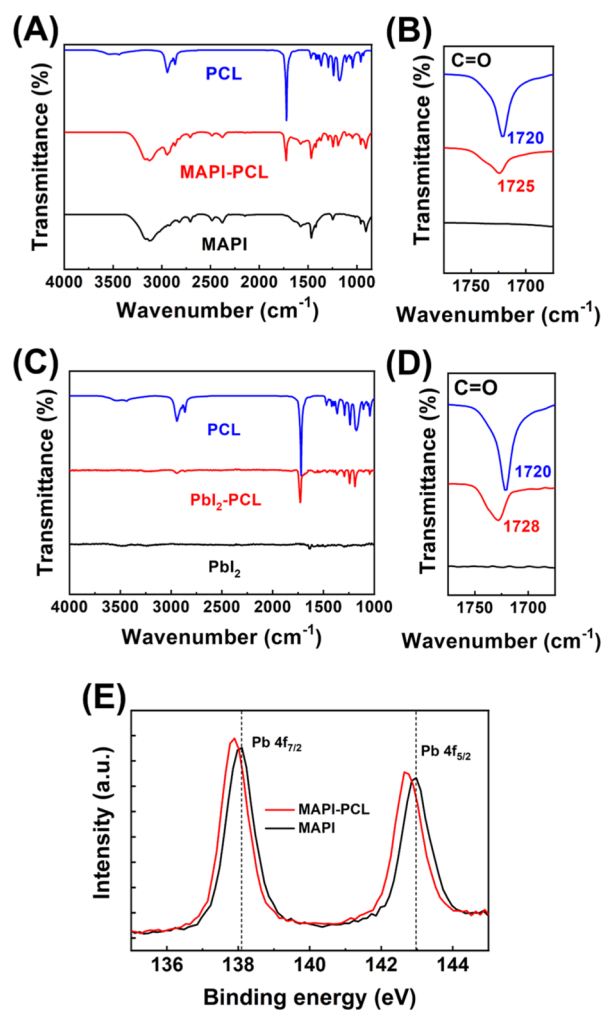


Figure 2. Chemical interaction between PCL polymer and MAPI perovskite. (A,B) ATR-FTIR spectra of PCL-passivated MAPI (red) compared with pristine MAPI (black) and PCL (blue). (C,D) ATR-FTIR spectra of PbI_2 mixed with PCL (red) compared with pure PbI_2 (black) and PCL (blue). (E) XPS spectra for Pb 4f of MAPI with (red) and without (black) PCL passivation.

Meanwhile, XPS measurements show a red shift of the binding energy of the Pb 4f orbital in the MAPI perovskite thin film upon the incorporation of PCL (Figure 2E), while those for C 1s, N 1s, and I 3d orbitals remained unchanged (Figure S3), again confirming the strong interaction between the PCL and MAPI perovskite through Pb^{2+} .

Generally, when the polymer is blended in a thin film medium, it can be phase-separated and segregated at the top and/or bottom interfaces with air and substrates driven by the interfacial energy. To determine whether such an unfavorable interfacial macrosegregation of the polymer occurs in the PCL-incorporated MAPI perovskite thin film, the PCL-containing MAPI thin film (2 mg/mL PCL) prepared on a Au-coated Si substrate was subjected to the PM-IRRAS analysis, which primarily probes the molecular vibration of thin films in close proximity to the bottom substrate interface.^{64,65} In fact, we find that there was no sign of PCL-related spectral features in the obtained PM-IRRAS data (Figure S4), suggesting that negligible macroscale segregation of PCL occurs at the perovskite/bottom substrate interface.

Perovskite GBs Passivation by the PCL Polymer. The suggested notion of perovskite GB passivation by PCL was

corroborated by identifying the distribution of PCL in the intergranular area between perovskite grains *via* the lateral scanning force AFM: the topographical AFM micrographs of MAPI thin films without and with PCL (2 mg/mL) showed similar surface morphologies (Figure 3A,B), while the lateral-force micrographs featured distinctly softer areas (*i.e.*, higher voltage in the micrograph scale) at the GBs only in the samples containing PCL (Figures 3A,B and S5). Consistently, in the line profiles of the lateral-force AFM scan obtained from the marked lines on Figure 3A,B, the distinct peaks corresponding to the softer medium were evident at the GBs in the samples containing PCL while a relatively flat profile was observed for the pure MAPI without PCL (Figure 3C). This result provides evidence of the dispersion of the softer PCL polymer primarily at the perovskite GBs. Meanwhile, it is noted that the friction-mode AFM data does not exclude the possibility of the presence of the ultrathin PCL passivation layer on the exposed top grain surface, which should be, again, beneficial for protecting MAPI grains against moisture and ion migration.^{21,22,66}

The presence of PCL at the GB regions was further revealed in detail by TEM (Figure 3D,E): The perovskite GBs without incorporated PCL appears faint with some apparent defects created by the high-energy electron beam (Figure 3D), but the PCL-passivated GBs (2 mg/mL PCL) display distinct light-colored regions between darker crystal grains, suggesting that the PCL polymer fills the entire region of GBs. High-resolution TEM (HRTEM) lattice imaging focusing on the GB regions with a higher magnification clearly shows that while no obvious amorphous region is observed at the boundaries of the highly crystalline perovskite grains in the pure MAPI sample (Figure 3F), the amorphous regions were highly visible at the intergranular areas in the PCL-incorporated MAPI sample (Figure 3G). Considering the intrinsically amorphous nature of the PCL polymer (Figure S6), the results confirm the distribution of the PCL at the GBs of the perovskite films, as opposed to the formation of large independent aggregated polymer domains. Meanwhile, the lattice planes visible within the highly crystalline grains (Figure 3F,G) are identified as (220) and (310) planes of the tetragonal MAPI structure in both passivated and nonpassivated samples. It is noted that the passivation of perovskite GBs by PCL was consistently observed in other low and high PCL concentrations as well (1 and 4 mg/mL; Figure S7). These results prove that the dispersion of PCL occurs mainly at the intergranular regions between the MAPI perovskite grains as an ultrathin polymer coating on the grain surface, suggesting that the PCL added in MAPI is primarily passivating the perovskite GBs to provide a beneficial barrier against moisture and diffusion of ions.

The consideration of the polymer radius of gyration (R_g) indicates that the observed PCL GB passivation thickness for 2 mg/mL of PCL concentration corresponds to 1–2 polymer monolayers: We estimated that R_g of our PCL is *ca.* 1.77 nm at the unperturbed condition (see Supporting Information; page S9), indicating that the thickness of an unperturbed PCL monolayer would be *ca.* 3.54 nm (*i.e.*, $2R_g$). Because of the geometrical confinement effect^{67,68} caused by the smaller GB channel width (~ 1.5 – 3.5 nm, Figure 3G) than $2R_g$, the linear polymer chain is expected to have a flattened conformation, essentially reducing R_g along the plane-normal direction of the grain surface (Figure 4). In this case, only ~ 1 – 2 monolayers of the stretched PCL macromolecules are estimated to fill the GBs, effectively passivating the grains while minimally interfering with the inter-grain charge transport. This horizontally stretched

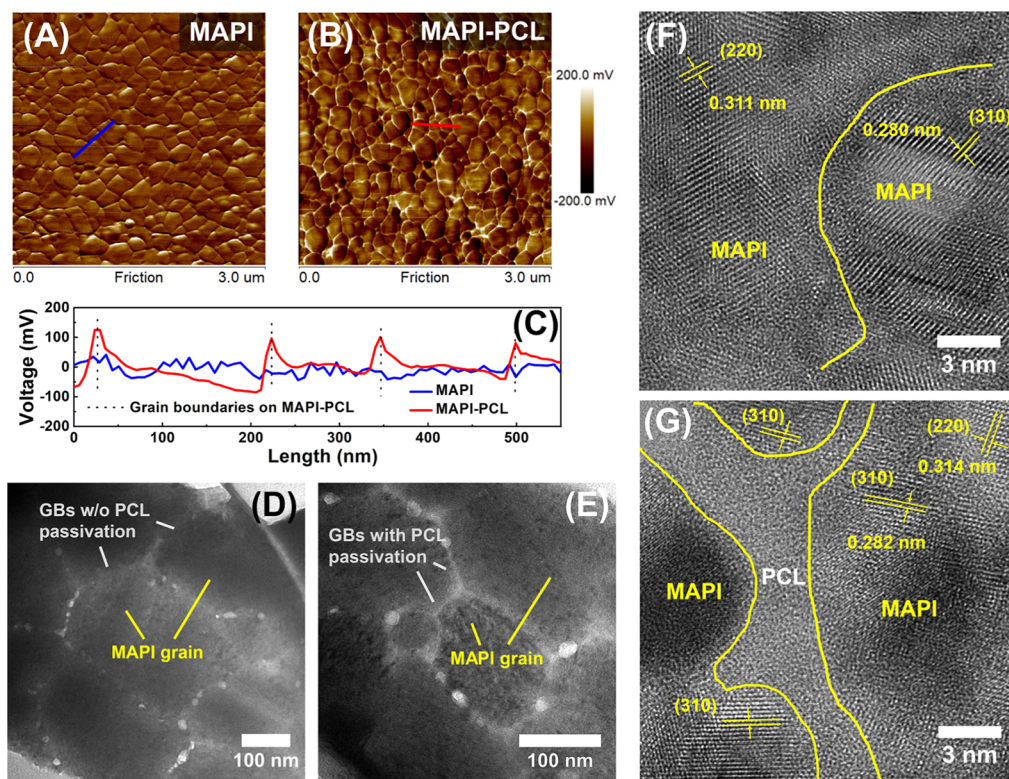


Figure 3. Identification of PCL passivation on perovskite GBs. Topographical lateral force (friction-mode) AFM micrographs of MAPI thin films without PCL (A) and with PCL incorporation (B). (C) Lateral deflection strength profiles along the lines marked in (A,B). Low-magnification TEM and HRTEM micrographs of pristine (D,F) and PCL-passivated (E,G) MAPI thin films.

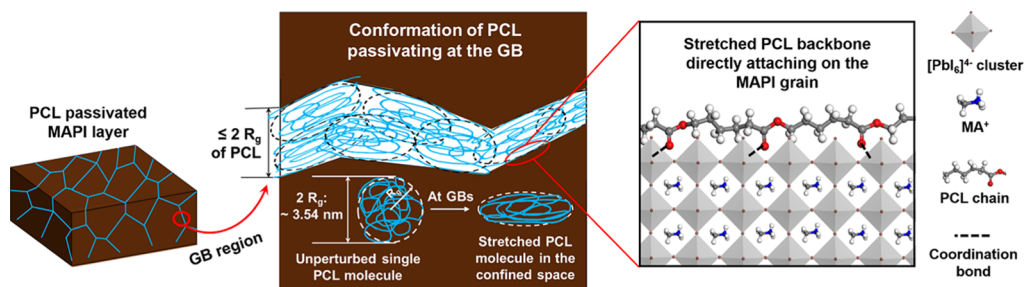


Figure 4. Schematic describing the stretched conformation and direct backbone attachment of monolayer PCL macromolecules to perovskite GBs *via* the coordination between the electron-donating C=O in ester groups on the PCL backbone and the electron-accepting Pb^{2+} of the perovskite grain surface.

chain conformation along the grain surface is expected to facilitate the PCL backbones to more closely interact with the grain surface, enabling the direct backbone attachment to the MAPI grain, mediated by the backbone C=O group in the PCL chain (Figure 4).

Overall, we postulate that the formation of the PCL GB passivation layer follows the following steps. First, during the initial growth of perovskite crystallites, some PCL is expected to act as heterogeneous nuclei. As the MAPI grains grow, the majority of the polymer is now being populated in the narrowing intergranular region between the growing MAPI crystallites because of its good affinity and ability to coordinate with MAPI surfaces. At the same time, the polymer chains are stretched because of the confinement effect and subsequently flattened chain conformation. These in turn enable the PCL polymer to be distributed uniformly along the MAPI GBs throughout the film interior without forming the macrosegregation at the bottom and top MAPI film interfaces. Compared with other

polymer additives reported previously wherein long, side branch groups were responsible for the interaction with the MAPI grain,^{36,38} the strong, direct attachment of the PCL chain backbone to the perovskite, realized *via* the adduct formation between the C=O on ester groups of the stretched PCL backbone and Pb atom in MAPI, minimizes the possible polymer steric hindrance and thus promotes a much closer attachment of the PCL backbone onto the MAPI grains, providing a more effective passivation of the MAPI grain surface and, eventually, significantly improved performance and environmental stabilities of MAPI perovskites and PSCs as we show next.

Optical Properties and PV Performance of PCL Passivated MAPI and PSCs. We first conducted steady-state PL measurements to determine the effect of the PCL additive on the radiative recombination characteristics of the photoexcited charge carriers in the MAPI thin film. The pristine and PCL-added (2 mg/mL) MAPI thin films with nominally identical

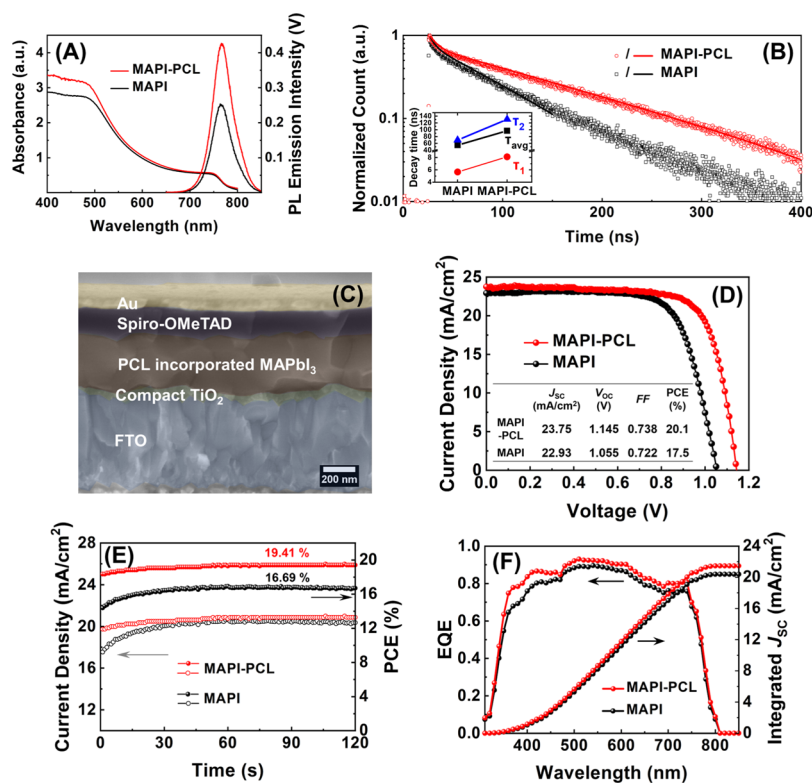


Figure 5. Optical and PV characteristics of pristine and PCL-passivated MAPI thin films. (A) UV–visible and steady-state PL spectra. (B) Temporal PL intensity decay profiles with an inset displaying extracted PL lifetimes. (C) False-colored cross-sectional SEM micrograph of a planar n–i–p PSC with a PCL-passivated MAPI active layer. (D) J – V characteristics with corresponding PV performance parameters (inset table). (E) Temporal profiles of steady-state PCE and J_{mpp} under AM1.5G 1 Sun illumination. (F) EQE spectra with integrated J_{sc} of the champion pristine and PCL-incorporated MAPI PSCs.

thicknesses were used, which were confirmed by the nearly identical ultraviolet (UV)–visible absorption spectra obtained from both samples, especially at the wavelengths above 500 nm (Figure 5A). Despite a similar film thickness, the PL data show that the emission intensity in the sample with the PCL GB passivation was increased by nearly 70% compared with that from the nonpassivated, pristine MAPI film (Figure 5A), providing clear evidence that the nonradiative recombination associated with defects and traps originating from the MAPI GB region has been effectively suppressed by the addition of the PCL polymer. Simultaneously, the PL spectra did not show any noticeable change in the peak position, indicating that the PCL passivation *via* the Lewis acid–base adduct formation with MAPI did not alter the optical bandgap of MAPI perovskites.

The recombination dynamics of photoexcited charge carriers, examined by the time-resolved PL measurement, shows significantly prolonged charge carrier lifetimes in the MAPI perovskite upon the incorporation of PCL. The temporal PL decay characteristics (at an emission peak of 765 nm) of the PCL-passivated and pristine MAPI perovskites (Figure 5B) were analyzed by the biexponential decay model with fast and slow components having time constants of τ_1 and τ_2 , respectively. The faster decay component (typically, $\tau_1 < \sim 20$ ns) in the model is generally attributed to the trapping of charge carriers in defect states while the slower decay components ($\tau_2 > \sim 20$ ns) to the direct bimolecular radiative recombination in the bulk.^{35,69} We find that both time constants were rendered significantly longer in the PCL-passivated MAPI than in the nonpassivated counterpart; with the addition of PCL, τ_1 increased from 5.6 to 8.1 ns and τ_2 from 69.5 to 130.7 ns, with

the average lifetime (τ_{avg}) increasing from 54.7 to 97.0 ns (Figure 5B inset and Table S1), signifying far fewer charge trapping sites and an overall much improved quality of the MAPI film enabled by the effective PCL passivation of the MAPI perovskite GB, thus subsequently leading to improved optoelectronic properties of the MAPI perovskite thin film.

We evaluated the PV performance of PCL-passivated MAPI perovskites and found a significant improvement of PCE primarily driven by enhanced V_{oc} . We used the n–i–p planar PSC architecture consisting of, from top to bottom, Au/Spiro-OMeTAD/MAPI (with or without PCL)/c-TiO₂/FTO in which Spiro-OMeTAD and c-TiO₂ served as the HTL and electron transport layer (ETL), respectively (Figure 5C). The illuminated J – V characteristics of champion PSCs made with or without a PCL polymer additive (2 mg/mL), measured under a simulated solar illumination (AM1.5G, 1 sun), are provided in Figure 5D. The corresponding PV performance parameters (Figure 5D inset) revealed that the reference MAPI PSC without PCL had a PCE of 17.5% with a short circuit density (J_{sc}) of 22.93 mA/cm², V_{oc} of 1.055 V, and fill factor (FF) of 0.722. Significantly, once PCL was incorporated, PCE was enhanced to 20.1% with J_{sc} , V_{oc} , and FF all also increased to 23.75 mA/cm², 1.145 V, and 0.738, respectively, among which the extent of V_{oc} enhancement being the most pronounced. The significantly increased V_{oc} can be generally ascribed to a commensurately suppressed charge carrier recombination,^{12,32,70} which is consistent with the prolonged charge carrier lifetime revealed by the time-resolved PL measurement, highlighting the importance of effective defect passivation of GBs and improved grain quality in the active MAPI perovskite

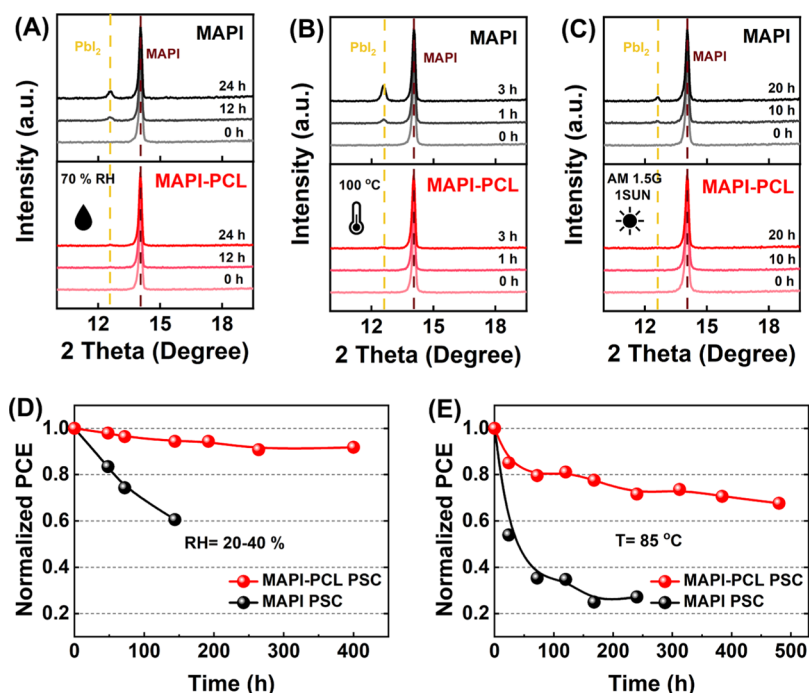


Figure 6. Stabilities of pristine and PCL-passivated MAPI perovskite thin films and PSCs. The evolution of XRD spectra under the continuous exposure to (A) moisture (70% RH, 25 °C, 24 h), (B) heat (dry Ar atmosphere at 100 °C, 3 h), and (C) light (AM1.5G 1 Sun, encapsulated in thin layer of PMMA, 20 h), respectively. Evolution of PCE of unencapsulated PSCs with respect to the exposure time in (D) ambient air (RH of 20–40%, room temperature, dark), and (E) heat (85 °C, Ar atmosphere, dark). The solid lines are guides for the eye only.

layer for achieving an improved PV performance. The relatively minor, yet appreciable increases of J_{SC} and FF can be also understood in the same manner *via* the reduced charge carrier recombination enabled by the efficient passivation of defect-concentrated GBs by PCL, which significantly reduces the charge trap density and prevents the recombination loss of photogenerated carriers.

In order to provide detailed information on the effect of the PCL additive concentration on the PV performance of MAPI PSCs, we built devices by using MAPI layers with varying concentrations of incorporated PCL, from 0 mg/mL (reference), 1 mg/mL, 2 mg/mL, and to 4 mg/mL. The device using the least PCL (1 mg/mL) showed the best PCE of 18.4% (average: $17.7 \pm 0.7\%$), which is higher than that of the reference MAPI devices without PCL incorporation (highest: 17.5%, average: $16.5 \pm 0.6\%$), but lower than the 20.1% champion PCE (average: $18.9 \pm 0.7\%$) of the optimally PCL-passivated MAPI PSCs (2 mg/mL) (Figure S8 and Table S2). J_{SC} , V_{OC} , and FF all also exhibited a similar PCL-concentration dependence as PCE (Figure S8 and Table S2). Meanwhile, the further increased PCL concentration to 4 mg/mL rather adversely affected the PV performance, with the best device PCE now being reduced to 16.0% (average: $14.9 \pm 1.0\%$), even lower than that of the reference MAPI device without PCL, along with the decreased corresponding J_{SC} , V_{OC} , and FF values as well (Figure S8 and Table S2). This likely results from an excessive PCL aggregation along MAPI GBs, which insulates the charge carrier transport and increases the resistance of the active MAPI layer.

The improved PCE of MAPI PSCs by the PCL passivation was accompanied by similar increases in the steady-state PCE and EQE. Steady-state PCE was measured by subjecting devices to the bias voltage corresponding to the maximum power point (V_{mpp}) in the illuminated J – V characteristics under AM1.5 G 1

Sun illumination and monitoring the corresponding J outputs (J_{mpp}) over a 2 min period. Steady-state PCE and J_{mpp} of MAPI PSCs with and without PCL passivation (2 mg/mL) are plotted in Figure 5E. A stabilized PCE of 19.41% ($J_{mpp} = 20.87 \text{ mA/cm}^2$) was reached upon the illumination of the PCL-passivated MAPI PSC, as opposed to a PCE of 16.69% (20.36 mA/cm^2) in the reference MAPI PSC without PCL (Figure 5E). We note that the stabilized PCE values were somewhat lower than those directly extracted from the J – V characteristics. Nevertheless, the results highlight the enhancement of PCE in MAPI PSCs enabled by the PCL GB passivation.

Similarly, the PCL passivation improved the overall EQE of the MAPI PSC, but, more significantly in the shorter wavelength region (Figure 5F). Given the nearly identical optical absorption between pristine and PCL-passivated MAPI perovskites in the wavelength range longer than 550 nm (Figure 5A), the improved EQE of the passivated PSC in this longer wavelength range reflects the improvement of the perovskite grain quality³⁰ with reduced trap densities and suppressed nonradiative recombination. In the nonpassivated PSC, the presence of mid-gap trap states, likely originating from uncoordinated dangling bonds at the GBs, induces the recombination before their collections, resulting in the reduced number of collected free charge carriers per absorbed photons (*i.e.*, reduced EQE). On the other hand, the increase of EQE at shorter wavelengths (<500 nm) by the PCL passivation is more likely related to the enhanced light absorption in that particular wavelength range as shown in Figure 5A. While the exact origin of this improved light absorption in the shorter wavelength range needs further investigation, we speculate that because of the lower relative dielectric constant (~ 3) of the polymer than that of the MAPI perovskite (~ 25.7),⁷¹ the PCL passivation at GBs might increase the dielectric contrast between MAPI grains and enhance the Rayleigh scattering, whose intensity (I_{Rayleigh})

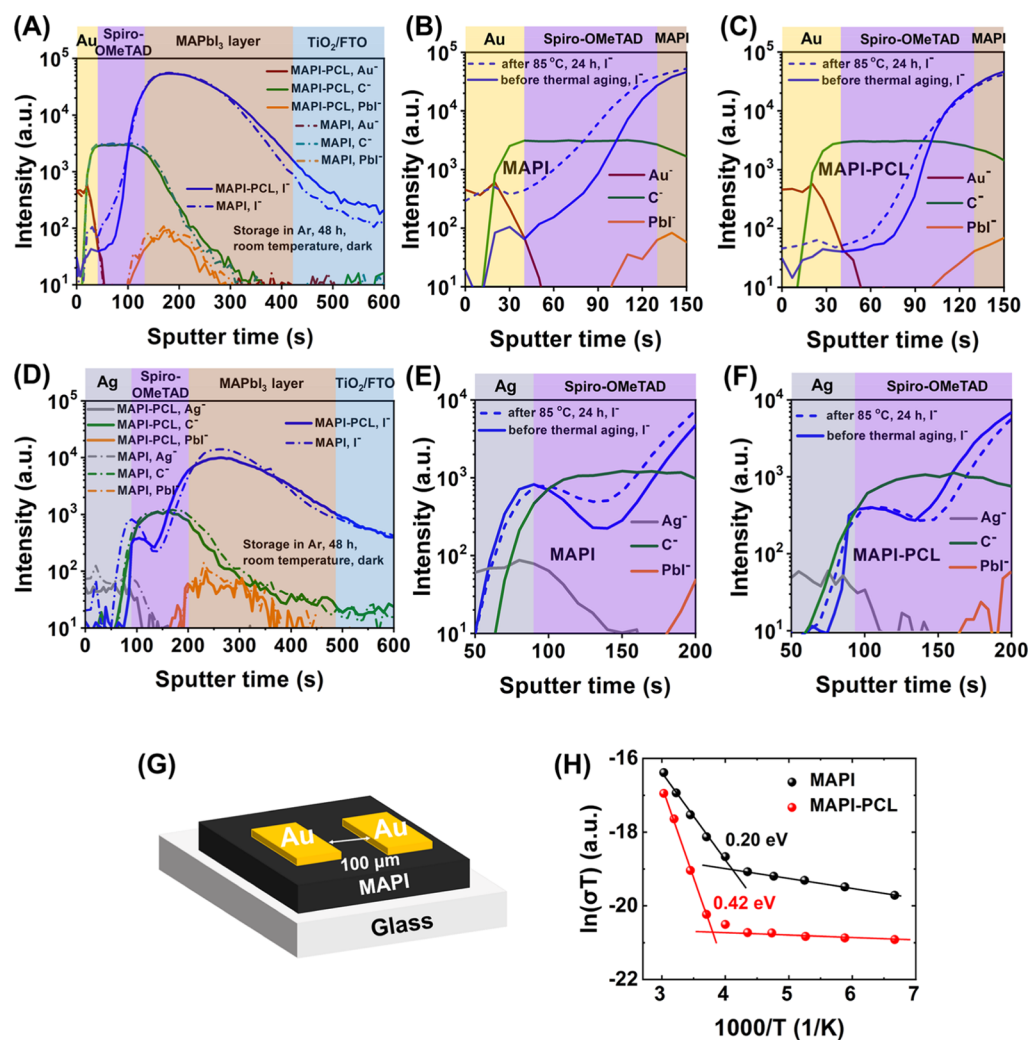


Figure 7. TOF-SIMS depth profiles depicting the effect of PCL on the iodide ion distribution in PSCs with the Au (A–C) or Ag (D–F) electrode. (A,D) Comparison of iodide distribution in PSCs without (MAPI) and with PCL (MAPI–PCL) after the storage in Ar for 48 h (room temperature, dark). The iodide ion distribution around the top HTL region in MAPI (B,E) and MAPI–PCL (C,F) before and after an additional thermal annealing at 85 °C for 24 h. (G) Schematic device structure used for characterizing the ion migration activation energy in MAPI thin films. (H) Temperature-dependent electrical conductivity (σ) of MAPI thin films with (solid red circle) and without PCL passivation (solid black circle), where the slopes of lines indicate the charge (*i.e.*, electron at low temperature and ion at high temperature) transport activation energy.

increases with decreasing wavelength (λ) following $I_{\text{Rayleigh}} \sim \lambda^{-4}$ relation,⁷² and thus increasing the overall optical absorption of the MAPI film. Overall, the J_{SC} estimated by integrating the EQE spectrum over the standard AM1.5G solar spectrum reached 21.85 mA/cm² in the PCL-passivated MAPI device as compared with 20.73 mA/cm² of the reference device without PCL (Figure 5F), both of which being slightly lower (<10%) than the values directly extracted from J – V characteristics but largely consistent in the trend.

We note that the difference between the measured and integrated J_{SC} indicates the existence of the hysteresis in the PV J – V characteristics, which mainly result from the planar structure of our devices without the mesoporous ETL layer.⁷³ However, the hysteresis was found to be reduced by the PCL passivation, based on the hysteresis index (HI) calculated from the measured reverse and forward J – V characteristics of the pristine and PCL-passivated PSCs (Figure S9) using the following equation^{73–75}

$$\text{HI} = \frac{J_{\text{rev}}(0.5/0.8V_{\text{OC}}) - J_{\text{for}}(0.5/0.8V_{\text{OC}})}{J_{\text{rev}}(0.5/0.8V_{\text{OC}})}$$

where $J_{\text{rev}}(0.5/0.8 V_{\text{OC}})$ and $J_{\text{for}}(0.5/0.8 V_{\text{OC}})$ are the currents at either 50⁷⁵ or 80%⁷³ of the V_{OC} during the reverse and forward J – V scans, respectively. No matter what percent of V_{OC} was chosen for the calculation, the results all showed the reduction of HI (from 0.146 to 0.041 for 0.5 V_{OC} and from 0.386 to 0.133 for 0.8 V_{OC}) after the PCL GB passivation. The attenuated hysteresis can be largely attributed to the reduced charge trap densities as well as the anticipated suppression of ion migration²¹ in our PSCs by the PCL GB passivation.

In the next section, we demonstrate that this enhanced PCE is accompanied by significantly improved performance stabilities and, more importantly, suppression of ion migration under environmental stresses, which we understand are enabled by the suggested unique, direct backbone attachment of PCL polymer chains on MAPI GBs.

Improvement of Chemical Stability. The chemical stabilities of PCL-incorporated MAPI thin films (2 mg/mL)

have been evaluated and compared with pristine MAPI thin films under various controlled, continuous environmental stresses, including moisture, heat, and light by monitoring the responding structural evolutions using XRD. The humidity stability (at RH \sim 70% and room temperature) tested over a 24 h period shows that there is a clear growth of the PbI_2 crystal in the pristine MAPI as evidenced by the increase of the PbI_2 (110) peak intensity, indicating the expected and well-documented degradation of MAPI under the extensive exposure to moisture^{12,33,35,76–78} (Figures 6A and S10). On the other hand, no obvious PbI_2 structure has been found in the PCL-incorporated MAPI even after 24 h of exposure, highlighting the excellent moisture repelling ability of the PCL-passivated MAPI sample (Figures 6A and S10). Likewise, the PCL-passivated MAPI exhibited significantly enhanced stabilities under heat and light; XRD showed no sign of the growth of PbI_2 for the both cases during 3 h continuous heating (at 100 °C in an Ar-filled glovebox) (Figures 6B and S11) or 20 h continuous illumination under AM1.5G 1 sun condition (encapsulated by PMMA to exclude other ambient factors) (Figures 6C and S12). In contrast, the pristine MAPI exhibited the decomposition of MAPI to PbI_2 in the both circumstances as indicated by the increasing intensity of the PbI_2 (001) peak in XRD spectra. The results from these three experiments clearly confirm that the effective GB passivation by PCL enabled the comprehensive enhancement of environmental stabilities of MAPI perovskites against moisture, heat, and light by suppressing the degradation of MAPI perovskite thin films, which, in general, start and then spread from the intergranular area between MAPI grains.¹²

The observed structural stability of PCL-passivated MAPI thin films under environmental stresses directly translates into an improved stability of the corresponding PV device performance. We monitored the PV performances of MAPI PSCs with and without a PCL additive over the 400 h, ambient-air, dark storage period (room temperature, RH = 20–40%) (Figures 6D and S13). The results show that the PCE of pristine MAPI device dropped down to 60% of its initial value in less than 150 h with the obvious degradation of J – V characteristics (Figure S14A). The MAPI PSC with PCL passivation on the other hand maintained over 90% of its initial PCE for more than 400 h storage period with a minimal degradation in J – V characteristics (Figure S14B).

Similarly, the PCL passivation enhanced the thermal stability of the PCE in MAPI PSCs; during the course of continuous heating at 85 °C in a glovebox, the MAPI PSC without PCL displayed a fast decay of PCE down to less than 60% of its initial value only after 24 h (Figures 6E and S15). In contrast, the PCL-passivated MAPI PSC maintained over 80% of its initial PCE in 24 h period and retained 65% of its initial value even after 480 h heat exposure. The comparison of J – V characteristics before and after 240 h heating clearly indicates the degradation of the pristine MAPI PSC driven by the emergence of “S-shape”, which is absent in the PCL-passivated MAPI PSC (Figure S16). The development of the S-shape in the solar cell J – V characteristics is generally caused by an increased series resistance within the device, for example, *via* the oxidative degradation of the electrode-active layer interface. Indeed in MAPI PSCs, a major cause of the fast PV performance loss has been largely associated with the degradation of the Spiro-OMeTAD HTL, which has been explained by the chemical reduction of Spiro-OMeTAD and subsequent reduction in its hole conductivity by the iodide ions migrating from the active perovskite layer.^{46,79} The fact that the PCL-passivated MAPI PSC did not develop the S-shape in

the J – V characteristics after being subjected to environmental stresses, especially even after an extended period of heating, strongly suggests that the GB passivation by PCL in the active MAPI layer also actually suppresses the detrimental iodine ion migration, which is prone to occur more easily under the elevated temperature, from the MAPI layer to the electrode interfaces, thus, degrading the Spiro-OMeTAD HTL.

Ion Migration Suppression and Activation Energy (E_a) Increase of PCL-Passivated MAPI PSCs. We confirmed the suggested notion of suppressed iodine ion migration enabled by the PCL passivation by performing compositional depth-profiling *via* TOF-SIMS of pristine and PCL-incorporated MAPI PSCs with either Au or Ag top electrode measurements (see the Experimental Section for detailed experimental parameters such as type and energy of sputter and probe ion sources; sputtering times, *etc.*). The compositional depth-profiles of pristine and PCL-passivated MAPI PSCs with Au top electrodes subjected to the shelf storage (Ar atmosphere, room temperature, dark) for 48 h and additional thermal aging for 24 h (85 °C, Ar) are provided in Figure 7A–C. The results clearly exhibited a lower iodine intensity in the Spiro-OMeTAD HTL region for the PCL-passivated MAPI PSC after storage, when compared with the pristine MAPI PSC (Figure 7A), while other components, such as Au^- , C^- , and PbI^- , showed relatively comparable intensities for the both pristine and PCL-passivated MAPI PSCs. The suppression of iodine migration in MAPI PSCs by the PCL GB passivation was much more pronounced under the extra thermal aging; after the additional thermal aging for only 24 h, the I^- counts at the Au/Spiro-OMeTAD layer interface (sputter time at 40 s) have increased by \sim 600% in the pristine MAPI PSC (Figures 7B and S17A), which should lead to the rapid degradation of HTL and consequently increased series resistance, agreeing well with the observed fast PV performance decay and emergence of S-shape J – V characteristics in the pristine MAPI PSC after the thermal stress. On the contrary, the I^- counts at the interface in the PCL-passivated MAPI PSC have increased by only \sim 25% after the identical period of thermal stress (Figures 7C and S17B). To summarize the suppression effect, we further integrated the I^- count in the depth range from the middle of Au electrode to the center of the Spiro-OMeTAD layer (sputter time from 20 to 85 s), which represents the overall I^- accumulation in the Au electrode, Spiro-OMeTAD, and their interface regions (Figure S18A). The results indicate that: (1) after the storage for 48 h in Ar, the PCL-passivated PSC featured \sim 70% less I^- accumulation in those regions compared with the nonpassivated reference; (2) after the 85 °C heating for 24 h, the I^- counts increased by \sim 560% in the nonpassivated PSC, while a much attenuated, \sim 160% increase in the I^- counts was observed in the PCL-passivated PSC. Overall, these results show that the PCL passivation on MAPI GBs effectively retards the iodide diffusion from the MAPI layer toward the electrode and HTL, therefore significantly suppressing the ion migration-related PV performance degradation in MAPI PSCs.

We also find that the PCL passivation was effective in suppressing the iodide migration and accumulation toward the electrode interface in the MAPI PSC with the Ag top electrode. Ag electrodes are generally more cost effective for the practical application of MAPI PSCs but are less noble and, therefore, more vulnerable to the oxidative degradation, which can occur *via* the reaction with the iodide ions migrated from the active MAPI layer and the formation of an insulating AgI layer between the Ag and HTL, severely hindering the charge transport and

eventually harming the overall PV performance.^{47,80} Indeed, the compositional depth profile of a pristine MAPI PSC with an Ag electrode shows that a severe accumulation of iodine ions between Ag and Spiro-OMeTAD HTL after a 48 h shelf storage (Figure 7D), with the slightly increased Ag⁻ signal intensity at the Ag/Spiro-OMeTAD interface suggesting the formation of the AgI interlayer. These observations also indicate a very active diffusion of iodide ions in pristine MAPI PSCs with Ag electrodes without external driving forces.⁴⁷ Now, once PCL was incorporated in the MAPI PSC, there was a clear reduction of the I⁻ accumulation and the formation of the AgI layer at the Ag/Spiro-OMeTAD interface (sputter time at 90 s), as evidenced by the ~60% decrease of I⁻ peak intensity and the disappearance of the Ag⁻ peak, as well as the lowered I⁻ ion penetration into the Ag electrode as compared with the pristine MAPI PSC (Figure 7D). After the additional heating at 85 °C for 24 h, more I⁻ counts were observed in the Spiro-OMeTAD layer for the nonpassivated PSC (Figures 7E and S17C), and such a migration was suppressed by the PCL passivation (Figures 7F and S17D). Consistently, from the I⁻ counts integrated from the middle of the Ag electrode to the center of the Spiro-OMeTAD layer (sputter time: 45–145 s), we found that: (1) after 48 h storage in Ar, the passivated PSC showed a ~50% less accumulated I⁻ than the nonpassivated one and (2) the additional 24 h heating resulted in a further increase of I⁻ counts by ~25% in the nonpassivated PSC, while only ~3% increase of I⁻ was observed in the PCL-passivated one (Figure S18B).

We note that the iodine migration in PSCs without the external electric field is generally perceived to occur *via* (1) the decomposition of MAI into volatile HI formed in the MAPI layer under environmental stresses (*i.e.*, CH₃NH₃I → CH₃NH₂ + HI)⁴⁸ and (2) the subsequent diffusion of iodine ions into the HTL driven by the concentration gradient and the interaction with the back contact electrode.⁴⁷ The structural stabilities and compositional depth profiles we observed, with respect to various environmental stresses, suggest that the PCL GB passivation not only helped maintain the MAPI perovskite structure against the chemical decomposition but also suppressed the iodide ion diffusion through the active MAPI layer, signaling an increased ion migration activation energy within the MAPI layer by the PCL GB passivation.

We confirmed the PCL passivation-induced increase in ion migration activation energy by measuring the temperature-dependent electrical conductivities of the pristine and PCL-incorporated MAPI thin films between two lateral top electrical contacts (Figure 7G) and model them using a Arrhenius-type activation equation;^{14,31} the measured apparent conductivity of a given MAPI film is generally dominated by ion transport at high temperatures but at sufficiently low temperatures, the conductivity is rendered dominated by the electron transport as the physical ion motion freezes out. The long-channeled two lateral top contacts we employed also reduce the influence of electron conduction and emphasize the conduction contribution from ions.^{14,31} We extracted the charge transport activation energy, E_a , by fitting the measured temperature-dependent conductivity (σ) to the Nernst–Einstein equation: $\sigma(T) = (\sigma_0/T) \exp(-E_a/kT)$, with σ_0 , T , and k denoting temperature-independent pre-factor, temperature, and Boltzmann constant, respectively.⁸¹ In both pristine and PCL-passivated MAPI thin films, the measured σT when plotted against $1/T$ in a logarithmic scale clearly display linearity with two distinctive regions of different slopes (*i.e.*, E_a), thus confirming the validity

of the model as well as two different charge transport regimes, each being dictated by electron (low temperature) and ion (high temperature) transports (Figure 7H). From the slopes in the high-temperature regime, we find that the PCL passivation of MAPI drastically increased the E_a for ion migration to 0.42 eV, from 0.2 eV in the pristine MAPI, where the E_a for the pristine MAPI is largely consistent with the previously reported values.^{14,31} Additionally, the PCL passivation increased the threshold temperature for the onset of ion transport (*i.e.*, the critical temperature at which the slope changes in Figure 7H) by ~20–263 K from 243 K in the pristine MAPI. Both of these materials parameters are associated with the ion transport and provide unambiguous evidence that the PCL passivation of MAPI GBs significantly suppresses the detrimental iodide migration within the MAPI PSCs and therefore is responsible for the enhanced device PV performance stability under the tested environmental stresses.

CONCLUSIONS

We incorporated a new polymer additive PCL into MAPI perovskite thin films to passivate the perovskite GBs, where the stretched linear PCL polymer with C=O bonds along the backbone could directly coordinate with the Pb²⁺ in the MAPI perovskite crystal, thus enabling the direct backbone attachment of PCL to the MAPI and effective passivation of MAPI GB regions during the film preparation. The successful PCL GB passivation was shown to be highly effective in not only improving the optoelectronic properties and PV performance of MAPI PSCs through the effective defect passivation but also substantially enhancing the structural and performance stability of the MAPI perovskite and its PSCs against various environmental stresses. We attribute the demonstrated stability improvement of PSCs to the ability of PCL-passivated MAPI perovskites to maintain their structural integrity and, more importantly, to the suppressed ion migration toward the Spiro-OMeTAD HTL and the electrode in the regular n–i–p type PSC structure. We envision that this straightforward and effective PCL GB passivation strategy can help tackle the critical stability issues of OIHP materials and their optoelectronic devices, which in turn will advance the development and practical deployment of more environmentally stable high-performance PSCs.

ASSOCIATED CONTENT

Supporting Information

The Supporting Information is available free of charge at <https://pubs.acs.org/doi/10.1021/acs.chemmater.0c00995>.

Details on solution preparation for spin casting; additional XPS data; SEM images of MAPI films made without the antisolvent; XPS spectra of C 1s, N 1s and I 3d_{5/2}; PM-IRRAS data; additional AFM images; XRD data of PCL film; additional HRTEM images; calculation of the radius of gyration (R_g) of the PCL polymer; table summarizing fitted lifetime data; statistic figures and table of J – V characteristics; plots of forward and reverse J – V characteristics with hysteresis index; additional time-dependent perovskite XRD data against moisture, heat, and light; evolution of J – V characteristics and curves in moisture and heat; additional ToF-SIMS depth profile data; and histogram summarizing integration of I⁻ counts from the ToF-SIMS data (PDF)

■ AUTHOR INFORMATION

Corresponding Authors

Chang-Yong Nam – Department of Materials Science and Chemical Engineering, Stony Brook University, Stony Brook, New York 11794, United States; Center for Functional Nanomaterials, Brookhaven National Laboratory, Upton, New York 11973, United States; orcid.org/0000-0002-9093-4063; Email: cynam@bnl.gov

Miriam H. Rafailovich – Department of Materials Science and Chemical Engineering, Stony Brook University, Stony Brook, New York 11794, United States; Email: miriam.rafailovich@stonybrook.edu

Authors

Yuchen Zhou – Department of Materials Science and Chemical Engineering, Stony Brook University, Stony Brook, New York 11794, United States

Yifan Yin – Department of Materials Science and Chemical Engineering, Stony Brook University, Stony Brook, New York 11794, United States

Xianghao Zuo – Department of Materials Science and Chemical Engineering, Stony Brook University, Stony Brook, New York 11794, United States

Likun Wang – Department of Materials Science and Chemical Engineering, Stony Brook University, Stony Brook, New York 11794, United States; orcid.org/0000-0001-9115-0220

Tai-De Li – Advanced Science Research Center at the Graduate Center of the City University of New York, New York, New York 10031, United States

Yuanyuan Zhou – School of Engineering, Brown University, Providence, Rhode Island 02912, United States

Nitin P. Padture – School of Engineering, Brown University, Providence, Rhode Island 02912, United States; orcid.org/0000-0001-6622-8559

Zhenhua Yang – Department of Materials Science and Chemical Engineering, Stony Brook University, Stony Brook, New York 11794, United States

Yichen Guo – Department of Materials Science and Chemical Engineering, Stony Brook University, Stony Brook, New York 11794, United States; orcid.org/0000-0002-1637-4440

Yuan Xue – Department of Materials Science and Chemical Engineering, Stony Brook University, Stony Brook, New York 11794, United States

Kim Kisslinger – Center for Functional Nanomaterials, Brookhaven National Laboratory, Upton, New York 11973, United States

Mircea Cotlet – Center for Functional Nanomaterials, Brookhaven National Laboratory, Upton, New York 11973, United States

Complete contact information is available at:

<https://pubs.acs.org/10.1021/acs.chemmater.0c00995>

Notes

The authors declare no competing financial interest.

■ ACKNOWLEDGMENTS

The research was carried out at the Center for Functional Nanomaterials (CFN), Brookhaven National Laboratory (BNL), which is supported by the U.S. Department of Energy, Office of Basic Energy Sciences, under Contract no. DE-SC0012704. This work was also supported by the National Science Foundation NSF-1344267 Inspire program. C.-Y.N

acknowledges the support from the Global Research Laboratory (GRL) Program of the National Research Foundation (NRF) of Korea funded by the Ministry of Science, ICT and Future Planning (NRF-2017K1A1A2013153). Y.Z. and N.P.P. acknowledge the support from the National Science Foundation (no. OIA-1538893) and Office of Naval Research (N00014-17-1-2232). Y.Z. also acknowledges the funding support from NSF (no. OIA-1929019). The authors acknowledge the access to the facilities at Advanced Science Research Center, the City University of New York.

■ REFERENCES

- (1) Chen, Y.; He, M.; Peng, J.; Sun, Y.; Liang, Z. Structure and Growth Control of Organic-Inorganic Halide Perovskites for Optoelectronics: From Polycrystalline Films to Single Crystals. *Adv. Sci.* **2016**, *3*, 1500392.
- (2) Kojima, A.; Teshima, K.; Shirai, Y.; Miyasaka, T. Organometal Halide Perovskites as Visible-Light Sensitizers for Photovoltaic Cells. *J. Am. Chem. Soc.* **2009**, *131*, 6050–6051.
- (3) Yang, W. S.; Park, B.-W.; Jung, E. H.; Jeon, N. J.; Kim, Y. C.; Lee, D. U.; Shin, S. S.; Seo, J.; Kim, E. K.; Noh, J. H.; Seok, S. I. Iodide Management in Formamidinium-Lead-Halide-Based Perovskite Layers for Efficient Solar Cells. *Science* **2017**, *356*, 1376–1379.
- (4) Stranks, S. D.; Eperon, G. E.; Grancini, G.; Menelaou, C.; Alcocer, M. J. P.; Leijtens, T.; Herz, L. M.; Petrozza, A.; Snaith, H. J. Electron-Hole Diffusion Lengths Exceeding 1 Micrometer in an Organometal Trihalide Perovskite Absorber. *Science* **2013**, *342*, 341–344.
- (5) Nie, W.; Tsai, H.; Asadpour, R.; Blancon, J.-C.; Neukirch, A. J.; Gupta, G.; Crochet, J. J.; Chhowalla, M.; Tretiak, S.; Alam, M. A.; Wang, H.-L.; Mohite, A. D. High-Efficiency Solution-Processed Perovskite Solar Cells with Millimeter-Scale Grains. *Science* **2015**, *347*, 522–525.
- (6) Kim, H.-S.; Lee, C.-R.; Im, J.-H.; Lee, K.-B.; Moehl, T.; Marchioro, A.; Moon, S.-J.; Humphry-Baker, R.; Yum, J.-H.; Moser, J. E.; Grätzel, M.; Park, N.-G. Lead Iodide Perovskite Sensitized All-Solid-State Submicron Thin Film Mesoscopic Solar Cell with Efficiency Exceeding 9%. *Sci. Rep.* **2012**, *2*, 591.
- (7) Zheng, K.; Zhu, Q.; Abdellah, M.; Messing, M. E.; Zhang, W.; Generalov, A.; Niu, Y.; Ribaud, L.; Canton, S. E.; Pullerits, T. Exciton Binding Energy and the Nature of Emissive States in Organometal Halide Perovskites. *J. Phys. Chem. Lett.* **2015**, *6*, 2969–2975.
- (8) Xing, G.; Mathews, N.; Sun, S.; Lim, S. S.; Lam, Y. M.; Grätzel, M.; Mhaisalkar, S.; Sum, T. C. Long-Range Balanced Electron- and Hole-Transport Lengths in Organic-Inorganic $\text{CH}_3\text{NH}_3\text{PbI}_3$. *Science* **2013**, *342*, 344–347.
- (9) Leijtens, T.; Stranks, S. D.; Eperon, G. E.; Lindblad, R.; Johansson, E. M. J.; McPherson, I. J.; Rensmo, H.; Ball, J. M.; Lee, M. M.; Snaith, H. J. Electronic Properties of Meso-Superstructured and Planar Organometal Halide Perovskite Films: Charge Trapping, Photodoping, and Carrier Mobility. *ACS Nano* **2014**, *8*, 7147–7155.
- (10) Wehrenfennig, C.; Eperon, G. E.; Johnston, M. B.; Snaith, H. J.; Herz, L. M. High Charge Carrier Mobilities and Lifetimes in Organolead Trihalide Perovskites. *Adv. Mater.* **2014**, *26*, 1584–1589.
- (11) Zhou, Y.; Game, O. S.; Pang, S.; Padture, N. P. Microstructures of Organometal Trihalide Perovskites for Solar Cells: Their Evolution from Solutions and Characterization. *J. Phys. Chem. Lett.* **2015**, *6*, 4827–4839.
- (12) Zong, Y.; Zhou, Y.; Zhang, Y.; Li, Z.; Zhang, L.; Ju, M.-G.; Chen, M.; Pang, S.; Zeng, X. C.; Padture, N. P. Continuous Grain-Boundary Functionalization for High-Efficiency Perovskite Solar Cells with Exceptional Stability. *Chem* **2018**, *4*, 1404–1415.
- (13) Guerrero, A.; You, J.; Aranda, C.; Kang, Y. S.; Garcia-Belmonte, G.; Zhou, H.; Bisquert, J.; Yang, Y. Interfacial Degradation of Planar Lead Halide Perovskite Solar Cells. *ACS Nano* **2016**, *10*, 218–224.
- (14) Xing, J.; Wang, Q.; Dong, Q.; Yuan, Y.; Fang, Y.; Huang, J. Ultrafast Ion Migration in Hybrid Perovskite Polycrystalline Thin Films under Light and Suppression in Single Crystals. *Phys. Chem. Chem. Phys.* **2016**, *18*, 30484–30490.

- (15) Leijtens, T.; Eperon, G. E.; Noel, N. K.; Habisreutinger, S. N.; Petrozza, A.; Snaith, H. J. Stability of Metal Halide Perovskite Solar Cells. *Adv. Energy Mater.* **2015**, *5*, 1500963.
- (16) Bag, M.; Renna, L. A.; Adhikari, R. Y.; Karak, S.; Liu, F.; Lahti, P. M.; Russell, T. P.; Tuominen, M. T.; Venkataraman, D. Kinetics of Ion Transport in Perovskite Active Layers and Its Implications for Active Layer Stability. *J. Am. Chem. Soc.* **2015**, *137*, 13130–13137.
- (17) Wang, Q.; Chen, B.; Liu, Y.; Deng, Y.; Bai, Y.; Dong, Q.; Huang, J. Scaling Behavior of Moisture-Induced Grain Degradation in Polycrystalline Hybrid Perovskite Thin Films. *Energy Environ. Sci.* **2017**, *10*, 516–522.
- (18) Yun, J. S.; Kim, J.; Young, T.; Patterson, R. J.; Kim, D.; Seidel, J.; Lim, S.; Green, M. A.; Huang, S.; Ho-Baillie, A. Humidity-Induced Degradation via Grain Boundaries of $\text{HC}(\text{NH}_2)_2\text{PbI}_3$ Planar Perovskite Solar Cells. *Adv. Funct. Mater.* **2018**, *28*, 1705363.
- (19) Ji, F.; Pang, S.; Zhang, L.; Zong, Y.; Cui, G.; Padture, N. P.; Zhou, Y. Simultaneous Evolution of Uniaxially Oriented Grains and Ultralow-Density Grain-Boundary Network in $\text{CH}_3\text{NH}_3\text{PbI}_3$ Perovskite Thin Films Mediated by Precursor Phase Metastability. *ACS Energy Lett.* **2017**, *2*, 2727–2733.
- (20) Yin, W.-J.; Shi, T.; Yan, Y. Unique Properties of Halide Perovskites as Possible Origins of the Superior Solar Cell Performance. *Adv. Mater.* **2014**, *26*, 4653–4658.
- (21) Chen, J.; Lee, D.; Park, N.-G. Stabilizing the Ag Electrode and Reducing J-V Hysteresis through Suppression of Iodide Migration in Perovskite Solar Cells. *ACS Appl. Mater. Interfaces* **2017**, *9*, 36338–36349.
- (22) Shao, Y.; Fang, Y.; Li, T.; Wang, Q.; Dong, Q.; Deng, Y.; Yuan, Y.; Wei, H.; Wang, M.; Gruverman, A.; Shield, J.; Huang, J. Grain Boundary Dominated Ion Migration in Polycrystalline Organic-Inorganic Halide Perovskite Films. *Energy Environ. Sci.* **2016**, *9*, 1752–1759.
- (23) Rybin, N.; Ghosh, D.; Tisdale, J.; Shrestha, S.; Yoho, M.; Vo, D.; Even, J.; Katan, C.; Nie, W.; Neukirch, A. J.; Tretiak, S. Effects of Chlorine Mixing on Optoelectronics, Ion Migration, and Gamma-Ray Detection in Bromide Perovskites. *Chem. Mater.* **2020**, *32*, 1854–1863.
- (24) Kennard, R. M.; Dahlman, C. J.; Nakayama, H.; DeCrescent, R. A.; Schuller, J. A.; Seshadri, R.; Mukherjee, K.; Chabinyc, M. L. Phase Stability and Diffusion in Lateral Heterostructures of Methyl Ammonium Lead Halide Perovskites. *ACS Appl. Mater. Interfaces* **2019**, *11*, 25313–25321.
- (25) Pan, D.; Fu, Y.; Chen, J.; Czech, K. J.; Wright, J. C.; Jin, S. Visualization and Studies of Ion-Diffusion Kinetics in Cesium Lead Bromide Perovskite Nanowires. *Nano Lett.* **2018**, *18*, 1807–1813.
- (26) Gedamu, D.; Asuo, I. M.; Benetti, D.; Basti, M.; Ka, I.; Cloutier, S. G.; Rosei, F.; Nechache, R. Solvent-Antisolvent Ambient Processed Large Grain Size Perovskite Thin Films for High-Performance Solar Cells. *Sci. Rep.* **2018**, *8*, 12885.
- (27) Tsai, H.; Nie, W.; Cherkov, P.; Mack, N. H.; Xu, P.; Gupta, G.; Mohite, A. D.; Wang, H.-L. Optimizing Composition and Morphology for Large-Grain Perovskite Solar Cells via Chemical Control. *Chem. Mater.* **2015**, *27*, 5570–5576.
- (28) Liu, B.; Wang, S.; Ma, Z.; Ma, J.; Ma, R.; Wang, C. High-Performance Perovskite Solar Cells with Large Grain-Size Obtained by the Synergy of Urea and Dimethyl Sulfoxide. *Appl. Surf. Sci.* **2019**, *467–468*, 708–714.
- (29) Pham, N. D.; Tiong, V. T.; Yao, D.; Martens, W.; Guerrero, A.; Bisquert, J.; Wang, H. Guanidinium Thiocyanate Selective Ostwald Ripening Induced Large Grain for High Performance Perovskite Solar Cells. *Nano Energy* **2017**, *41*, 476–487.
- (30) Wang, R.; Xue, J.; Meng, L.; Lee, J.-W.; Zhao, Z.; Sun, P.; Cai, L.; Huang, T.; Wang, Z.; Wang, Z.-K.; Duan, Y.; Yang, J. L.; Tan, S.; Yuan, Y.; Huang, Y.; Yang, Y. Caffeine Improves the Performance and Thermal Stability of Perovskite Solar Cells. *Joule* **2019**, *3*, 1464–1477.
- (31) Li, X.; Zhang, W.; Wang, Y. C.; Zhang, W.; Wang, H. Q.; Fang, J. In-Situ Cross-Linking Strategy for Efficient and Operationally Stable Methylammonium Lead Iodide Solar Cells. *Nat. Commun.* **2018**, *9*, 3806.
- (32) Lee, J.-W.; Bae, S.-H.; Hsieh, Y.-T.; De Marco, N.; Wang, M.; Sun, P.; Yang, Y. A Bifunctional Lewis Base Additive for Microscopic Homogeneity in Perovskite Solar Cells. *Chem* **2017**, *3*, 290–302.
- (33) Niu, T.; Lu, J.; Munir, R.; Li, J.; Barrit, D.; Zhang, X.; Hu, H.; Yang, Z.; Amassian, A.; Zhao, K.; Liu, S. F. Stable High-Performance Perovskite Solar Cells via Grain Boundary Passivation. *Adv. Mater.* **2018**, *30*, 1706576.
- (34) Zhang, T.; Guo, N.; Li, G.; Qian, X.; Zhao, Y. A Controllable Fabrication of Grain Boundary PbI_2 Nanoplates Passivated Lead Halide Perovskites for High Performance Solar Cells. *Nano Energy* **2016**, *26*, 50–56.
- (35) Han, T.-H.; Lee, J.-W.; Choi, C.; Tan, S.; Lee, C.; Zhao, Y.; Dai, Z.; De Marco, N.; Lee, S.-J.; Bae, S.-H.; Yuan, Y.; Lee, H. M.; Huang, Y.; Yang, Y. Perovskite-Polymer Composite Cross-Linker Approach for Highly-Stable and Efficient Perovskite Solar Cells. *Nat. Commun.* **2019**, *10*, 520.
- (36) Bi, D.; Yi, C.; Luo, J.; Decoppet, J.-D.; Zhang, F.; Zakeeruddin, S. M.; Li, X.; Hagfeldt, A.; Grätzel, M. Polymer-Templated Nucleation and Crystal Growth of Perovskite Films for Solar Cells with Efficiency Greater than 21%. *Nat. Energy* **2016**, *1*, 16142.
- (37) Guo, Y.; Shoyama, K.; Sato, W.; Nakamura, E. Polymer Stabilization of Lead(II) Perovskite Cubic Nanocrystals for Semi-transparent Solar Cells. *Adv. Energy Mater.* **2016**, *6*, 1502317.
- (38) Zuo, L.; Guo, H.; deQuilettes, D. W.; Jariwala, S.; De Marco, N.; Dong, S.; DeBlock, R.; Ginger, D. S.; Dunn, B.; Wang, M.; Yang, Y. Polymer-Modified Halide Perovskite Films for Efficient and Stable Planar Heterojunction Solar Cells. *Sci. Adv.* **2017**, *3*, No. e1700106.
- (39) Xiang, W.; Chen, Q.; Wang, Y.; Liu, M.; Huang, F.; Bu, T.; Wang, T.; Cheng, Y.-B.; Gong, X.; Zhong, J.; Liu, P.; Yao, X.; Zhao, X. Improved Air Stability of Perovskite Hybrid Solar Cells via Blending Poly(Dimethylsiloxane)-Urea Copolymers. *J. Mater. Chem. A* **2017**, *5*, 5486–5494.
- (40) Dong, Q.; Wang, Z.; Zhang, K.; Yu, H.; Huang, P.; Liu, X.; Zhou, Y.; Chen, N.; Song, B. Easily Accessible Polymer Additives for Tuning the Crystal-Growth of Perovskite Thin-Films for Highly Efficient Solar Cells. *Nanoscale* **2016**, *8*, 5552–5558.
- (41) Huang, Z.; Hu, X.; Liu, C.; Tan, L.; Chen, Y. Nucleation and Crystallization Control via Polyurethane to Enhance the Bendability of Perovskite Solar Cells with Excellent Device Performance. *Adv. Funct. Mater.* **2017**, *27*, 1703061.
- (42) Zhang, C.-C.; Li, M.; Wang, Z.-K.; Jiang, Y.-R.; Liu, H.-R.; Yang, Y.-G.; Gao, X.-Y.; Ma, H. Passivated Perovskite Crystallization and Stability in Organic-Inorganic Halide Solar Cells by Doping a Donor Polymer. *J. Mater. Chem. A* **2017**, *5*, 2572–2579.
- (43) Sun, Y.; Wu, Y.; Fang, X.; Xu, L.; Ma, Z.; Lu, Y.; Zhang, W.-H.; Yu, Q.; Yuan, N.; Ding, J. Long-Term Stability of Organic-Inorganic Hybrid Perovskite Solar Cells with High Efficiency under High Humidity Conditions. *J. Mater. Chem. A* **2017**, *5*, 1374–1379.
- (44) Jiang, J.; Wang, Q.; Jin, Z.; Zhang, X.; Lei, J.; Bin, H.; Zhang, Z.-G.; Li, Y.; Liu, S. F. Polymer Doping for High-Efficiency Perovskite Solar Cells with Improved Moisture Stability. *Adv. Energy Mater.* **2018**, *8*, 1701757.
- (45) Dualeh, A.; Tétreault, N.; Moehl, T.; Gao, P.; Nazeeruddin, M. K.; Grätzel, M. Effect of Annealing Temperature on Film Morphology of Organic-Inorganic Hybrid Perovskite Solid-State Solar Cells. *Adv. Funct. Mater.* **2014**, *24*, 3250–3258.
- (46) Kim, S.; Bae, S.; Lee, S. W.; Cho, K.; Lee, K. D.; Kim, H.; Park, S.; Kwon, G.; Ahn, S. W.; Lee, H. M.; Kang, Y.; Lee, H. S.; Kim, D. Relationship between Ion Migration and Interfacial Degradation of $\text{CH}_3\text{NH}_3\text{PbI}_3$ Perovskite Solar Cells under Thermal Conditions. *Sci. Rep.* **2017**, *7*, 1200.
- (47) Zhang, T.; Meng, X.; Bai, Y.; Xiao, S.; Hu, C.; Yang, Y.; Chen, H.; Yang, S. Profiling the Organic Cation-Dependent Degradation of Organolead Halide Perovskite Solar Cells. *J. Mater. Chem. A* **2017**, *5*, 1103–1111.
- (48) Zhao, Y.; Zhou, W.; Tan, H.; Fu, R.; Li, Q.; Lin, F.; Yu, D.; Walters, G.; Sargent, E. H.; Zhao, Q. Mobile-Ion-Induced Degradation of Organic Hole-Selective Layers in Perovskite Solar Cells. *J. Phys. Chem. C* **2017**, *121*, 14517–14523.

- (49) Yang, Z.; Guo, Y.; Li, H.; Zhou, Y.; Zuo, X.; Yu, Y.; Pan, C.; Strzalka, J.; Nam, C.-Y.; Rafailovich, M. H. Roles of Interfacial Tension in Regulating Internal Organization of Low Bandgap Polymer Bulk Heterojunction Solar Cells by Polymer Additives. *Adv. Mater. Interfaces* **2018**, *5*, 1800435.
- (50) Zhou, Y.; Sternlicht, H.; Padture, N. P. Transmission Electron Microscopy of Halide Perovskite Materials and Devices. *Joule* **2019**, *3*, 641–661.
- (51) Eperon, G. E.; Burlakov, V. M.; Docampo, P.; Goriely, A.; Snaith, H. J. Morphological Control for High Performance, Solution-Processed Planar Heterojunction Perovskite Solar Cells. *Adv. Funct. Mater.* **2014**, *24*, 151–157.
- (52) Ahn, N.; Son, D.-Y.; Jang, I.-H.; Kang, S. M.; Choi, M.; Park, N.-G. Highly Reproducible Perovskite Solar Cells with Average Efficiency of 18.3 % and Best Efficiency of 19.7 % Fabricated via Lewis Base Adduct of Lead(II) Iodide. *J. Am. Chem. Soc.* **2015**, *137*, 8696–8699.
- (53) Jeon, N. J.; Noh, J. H.; Kim, Y. C.; Yang, W. S.; Ryu, S.; Seok, S. I. Solvent Engineering for High-Performance Inorganic-Organic Hybrid Perovskite Solar Cells. *Nature Mater* **2014**, *13*, 897–903.
- (54) Xiao, M.; Huang, F.; Huang, W.; Dkhissi, Y.; Zhu, Y.; Etheridge, J.; Gray-Weale, A.; Bach, U.; Cheng, Y.-B.; Spiccia, L. A Fast Deposition-Crystallization Procedure for Highly Efficient Lead Iodide Perovskite Thin-Film Solar Cells. *Angew. Chem., Int. Ed.* **2014**, *53*, 9898–9903.
- (55) Zuo, X.; Xue, Y.; Wang, L.; Zhou, Y.; Yin, Y.; Chuang, Y.-C.; Chang, C.-C.; Yin, R.; Rafailovich, M. H.; Guo, Y. Engineering Styrenic Blends with Poly(Lactic Acid). *Macromolecules* **2019**, *52*, 7547–7556.
- (56) Zuo, X.; Xue, Y.; Zhou, Y.; Yin, Y.; Li, T.-D.; Wang, L.; Chuang, Y.-C.; Chang, C.-C.; Rafailovich, M. H.; Guo, Y. The Use of Low Cost, Abundant, Homopolymers for Engineering Degradable Polymer Blends: Compatibilization of Poly(Lactic Acid)/Styrenics Using Poly(Methyl Methacrylate). *Polymer* **2020**, *186*, 122010.
- (57) Guo, Y.; Zuo, X.; Xue, Y.; Zhou, Y.; Yang, Z.; Chuang, Y.-C.; Chang, C.-C.; Yuan, G.; Satija, S. K.; Gersappe, D.; Rafailovich, M. H. Enhancing Impact Resistance of Polymer Blends via Self-Assembled Nanoscale Interfacial Structures. *Macromolecules* **2018**, *51*, 3897–3910.
- (58) Guo, Y.; He, S.; Yang, K.; Xue, Y.; Zuo, X.; Yu, Y.; Liu, Y.; Chang, C.-C.; Rafailovich, M. H. Enhancing the Mechanical Properties of Biodegradable Polymer Blends Using Tubular Nanoparticle Stitching of the Interfaces. *ACS Appl. Mater. Interfaces* **2016**, *8*, 17565–17573.
- (59) Rychter, M.; Baranowska-Korczyk, A.; Milanowski, B.; Jarek, M.; Maciejewska, B. M.; Coy, E. L.; Lulek, J. Cilostazol-Loaded Poly-(Epsilon-Caprolactone) Electrospun Drug Delivery System for Cardiovascular Applications. *Pharm. Res.* **2018**, *35*, 32.
- (60) Elzein, T.; Nasser-Eddine, M.; Delaite, C.; Bistac, S.; Dumas, P. FTIR Study of Polycaprolactone Chain Organization at Interfaces. *J. Colloid Interface Sci.* **2004**, *273*, 381–387.
- (61) Wang, Y.; Mahmoudi, T.; Rho, W.-Y.; Yang, H.-Y.; Seo, S.; Bhat, K. S.; Ahmad, R.; Hahn, Y.-B. Ambient-Air-Solution-Processed Efficient and Highly Stable Perovskite Solar Cells Based on $\text{CH}_3\text{NH}_3\text{PbI}_{3-x}\text{Cl}_x\text{-NiO}$ Composite with $\text{Al}_2\text{O}_3/\text{NiO}$ Interfacial Engineering. *Nano Energy* **2017**, *40*, 408–417.
- (62) Abdelmageed, G.; Mackeen, C.; Hellier, K.; Jewell, L.; Seymour, L.; Tingwald, M.; Bridges, F.; Zhang, J. Z.; Carter, S. Effect of Temperature on Light Induced Degradation in Methylammonium Lead Iodide Perovskite Thin Films and Solar Cells. *Sol. Energy Mater. Sol. Cells* **2018**, *174*, 566–571.
- (63) Hou, X.; Huang, S.; Ou-Yang, W.; Pan, L.; Sun, Z.; Chen, X. Constructing Efficient and Stable Perovskite Solar Cells via Interconnecting Perovskite Grains. *ACS Appl. Mater. Interfaces* **2017**, *9*, 35200–35208.
- (64) Kestell, J. D.; Mudiyansele, K.; Ye, X.; Nam, C.-Y.; Stacchiola, D.; Sadowski, J.; Boscoboinik, J. A. Stand-Alone Polarization-Modulation Infrared Reflection Absorption Spectroscopy Instrument Optimized for the Study of Catalytic Processes at Elevated Pressures. *Rev. Sci. Instrum.* **2017**, *88*, 105109.
- (65) Ye, X.; Kestell, J.; Kisslinger, K.; Liu, M.; Grubbs, R. B.; Boscoboinik, J. A.; Nam, C.-Y. Effects of Residual Solvent Molecules Facilitating the Infiltration Synthesis of ZnO in a Nonreactive Polymer. *Chem. Mater.* **2017**, *29*, 4535–4545.
- (66) Dunlap-Shohl, W. A.; Zhou, Y.; Padture, N. P.; Mitzi, D. B. Synthetic Approaches for Halide Perovskite Thin Films. *Chem. Rev.* **2019**, *119*, 3193–3295.
- (67) Magerl, D.; Philipp, M.; Metwalli, E.; Gutfreund, P.; Qiu, X.-P.; Winnik, F. M.; Müller-Buschbaum, P. Influence of Confinement on the Chain Conformation of Cyclic Poly(N-Isopropylacrylamide). *ACS Macro Lett.* **2015**, *4*, 1362–1365.
- (68) Shuto, K.; Oishi, Y.; Kajiyama, T.; Han, C. C. Aggregation Structure of Two-Dimensional Ultrathin Polystyrene Film Prepared by the Water Casting Method. *Macromolecules* **1993**, *26*, 6589–6594.
- (69) Shi, D.; Adinolfi, V.; Comin, R.; Yuan, M.; Alarousu, E.; Buin, A.; Chen, Y.; Hoogland, S.; Rothenberger, A.; Katsiev, K.; Losovyj, Y.; Zhang, X.; Dowben, P. A.; Mohammed, O. F.; Sargent, E. H.; Bakr, O. M. Low Trap-State Density and Long Carrier Diffusion in Organolead Trihalide Perovskite Single Crystals. *Science* **2015**, *347*, 519–522.
- (70) Son, D.-Y.; Lee, J.-W.; Choi, Y. J.; Jang, I.-H.; Lee, S.; Yoo, P. J.; Shin, H.; Ahn, N.; Choi, M.; Kim, D.; Park, N.-G. Self-Formed Grain Boundary Healing Layer for Highly Efficient $\text{CH}_3\text{NH}_3\text{PbI}_3$ Perovskite Solar Cells. *Nat. Energy* **2016**, *1*, 16081.
- (71) Brivio, F.; Walker, A. B.; Walsh, A. Structural and Electronic Properties of Hybrid Perovskites for High-Efficiency Thin-Film Photovoltaics from First-Principles. *APL Mater.* **2013**, *1*, 042111.
- (72) Rayleigh, L. XXXIV. On the Transmission of Light through an Atmosphere Containing Small Particles in Suspension, and on the Origin of the Blue of the Sky. *London, Edinburgh Dublin Philos. Mag. J. Sci.* **1899**, *47*, 375–384.
- (73) Kim, H.-S.; Park, N.-G. Parameters Affecting I–V Hysteresis of $\text{CH}_3\text{NH}_3\text{PbI}_3$ Perovskite Solar Cells: Effects of Perovskite Crystal Size and Mesoporous TiO_2 Layer. *J. Phys. Chem. Lett.* **2014**, *5*, 2927–2934.
- (74) Sanchez, R. S.; Gonzalez-Pedro, V.; Lee, J.-W.; Park, N.-G.; Kang, Y. S.; Mora-Sero, I.; Bisquert, J. Slow Dynamic Processes in Lead Halide Perovskite Solar Cells. Characteristic Times and Hysteresis. *J. Phys. Chem. Lett.* **2014**, *5*, 2357–2363.
- (75) Valles-Pelarda, M.; Hames, B. C.; García-Benito, I.; Almora, O.; Molina-Ontoria, A.; Sánchez, R. S.; Garcia-Belmonte, G.; Martín, N.; Mora-Sero, I. Analysis of the Hysteresis Behavior of Perovskite Solar Cells with Interfacial Fullerene Self-Assembled Monolayers. *J. Phys. Chem. Lett.* **2016**, *7*, 4622–4628.
- (76) Zhao, Y.; Wei, J.; Li, H.; Yan, Y.; Zhou, W.; Yu, D.; Zhao, Q. A Polymer Scaffold for Self-Healing Perovskite Solar Cells. *Nat. Commun.* **2016**, *7*, 10228.
- (77) Sun, Y.; Wu, Y.; Fang, X.; Xu, L.; Ma, Z.; Lu, Y.; Zhang, W.-H.; Yu, Q.; Yuan, N.; Ding, J. Long-Term Stability of Organic–Inorganic Hybrid Perovskite Solar Cells with High Efficiency under High Humidity Conditions. *J. Mater. Chem. A* **2017**, *5*, 1374–1379.
- (78) Li, B.; Fei, C.; Zheng, K.; Qu, X.; Pullerits, T.; Cao, G.; Tian, J. Constructing Water-Resistant $\text{CH}_3\text{NH}_3\text{PbI}_3$ Perovskite Films via Coordination Interaction. *J. Mater. Chem. A* **2016**, *4*, 17018–17024.
- (79) Jena, A. K.; Numata, Y.; Ikegami, M.; Miyasaka, T. Role of Spiro-Ometad in Performance Deterioration of Perovskite Solar Cells at High Temperature and Reuse of the Perovskite Films to Avoid Pb-Waste. *J. Mater. Chem. A* **2018**, *6*, 2219–2230.
- (80) Kato, Y.; Ono, L. K.; Lee, M. V.; Wang, S.; Raga, S. R.; Qi, Y. Silver Iodide Formation in Methyl Ammonium Lead Iodide Perovskite Solar Cells with Silver Top Electrodes. *Adv. Mater. Interfaces* **2015**, *2*, 1500195.
- (81) Bischoff, C.; Schuller, K.; Beckman, S. P.; Martin, S. W. Non-Arrhenius Ionic Conductivities in Glasses Due to a Distribution of Activation Energies. *Phys. Rev. Lett.* **2012**, *109*, 075901.